MR Microimaging of the Lung Using Volume Projection Encoding

Mark D. Shattuck, Sally L. Gewalt, Gary H. Glover, Laurence W. Hedlund, G. Allan Johnson

Radial acquisition (RA) techniques have been extended to produce isotropic, three-dimensional images of lung in live laboratory animals at spatial resolution down to 0.013 mm^3 with a signal-to-noise ratio of 30:1. The pulse sequence and reconstruction algorithm have been adapted to allow acquisition of image matrices of up to 256^3 in less than 15 min. Scan-synchronous ventilation has been incorporated to limit breathing motion artifacts. The imaging sequence permits randomizing and/or discarding selected views to minimize the consequences of breathing motion. The signal in lung parenchyma was measured as a function of flip angle (α) for different repetition times and found to follow the predictions for which there is an *optimum* excitation (Ernst) angle. A single T_1 relaxation value of 780 ± 54 ms fits all data from six guinea pigs at 2.0 T. This T_1 value parameterizes the signal and allows for *a priori* optimization, such as calculation of the Ernst angle appropriate for lung imaging.

Key words: MR microimaging, lung, projection encoding.

INTRODUCTION

MR microscopy has shown considerable utility in studies of a variety of organ systems. The advantage of following a single animal over time with the animal acting as its own control has proven most effective in reducing the cost and complexity in drug discovery (1). The ability to follow a specific organ at histological resolution has obvious implications in understanding basic mechanisms of disease (2). The effective application of MR microscopy to *in vivo* studies of any given organ system requires an integrated effort to optimize pulse sequence, physiological support, RF coils, and image reconstruction and analysis tools. Simply "turning up the knobs" on a clinical system to image an animal model is rarely sufficient to obtain microscopic resolution with meaningful signal-to-noise ratio. Moreover, coordination of all of these elements to permit routine microscopic studies requires significant effort beyond a demonstration that MR microscopy can be performed.

For the MR microscopist, the lung presents the single most challenging organ system to study. Roughly 80% of lung volume is air. As a consequence of the difference in magnetic susceptibility between lung tissue and air, a complicated spatially varying magnetic field is produced (3). This field inhomogeneity results in very short T_2*, with measured values ranging from 5–20 ms in humans (4). The movement of the lung due to breathing and cardiac motion creates further imaging problems (5). These problems are exacerbated in MR microscopy, where the practical resolution limits *in vivo* are generally imposed by either signal-to-noise limitations or biologic motion.

The applications of MR to the lung are many and varied. There are currently a number of potential treatments for asthma and emphysema. Unfortunately the metrics used in evaluating the efficacy of such treatments particularly in small animal models are very limited. The most common measure is a lung function study using spirometry. But the reserve capacity of the lung is so large that this metric is only useful for end stage disease. MR promises much more sensitive characterization through changes in density as well as the traditional parameters, T_2, T_2*, etc. (3, 4).

Projection encoding provides an elegant solution to all of the problems noted above. Lai and Lauterbur (6) suggested "true 3D imaging" in some of the earliest work in MRI. Several authors have demonstrated the benefits of direct encoding of the free induction decay (FID) to limit signal loss from short T_2* or diffusion (5, 7, 8). This exceptionally simple RF pulse scheme allows a very short interval between excitation and first point in the acquisition. For consistency, we refer to this interval as the echo time, or *TE*, because the *k*-space origin is acquired at this time. We have demonstrated previously the ability to acquire two-dimensional cardiac-gated projection images at microscopic resolution (5). In three-dimensional encoding, when cardiac gating is used, acquisition times are unacceptably long. Fortunately, three-dimensional projection encoding is inherently effective at suppressing motion artifacts, including cardiac motion, because there is heavy averaging in the center of *k*-space (7). We exploit this fact in order to limit the consequences of cardiac motion, and use scan-synchronous ventilation to limit the consequences of breathing motion. Furthermore, the simplicity of this three-dimensional sequence makes it possible to significantly reduce *TR* so that a 256^3 data set can be collected in less than 12 min. We describe here the development and integration of elements necessary for routine microimaging of the small animal lung: (a) to adapt 3D radial acquisition for MR microscopy, (b) to utilize scan-synchronous ventilation and view exclusion to minimize breathing motion artifacts, (c) to optimize specific RF coils; (d) to optimize RF pulses to maximize SNR while limiting acquisition

MRM 38:938–942 (1997)

From the Center for *In Vivo* Microscopy, Department of Radiology, Duke University Medical Center, Durham, North Carolina (M.D.S., S.L.G., L.W.H., G.A.J.); and Richard M. Lucas Center for Magnetic Resonance Imaging, Stanford University Medical Center, Stanford, California (G.H.G.).

Address correspondence to: Elaine G. Fitzsimons, M.S., Center for *In Vivo* Microscopy, Box 3302, DUMC, Durham, NC 27710-3302.

Received December 30, 1996; revised May 16, 1997; accepted May 22, 1997.

This work was supported in part by NIH NCRR #P41 RR0 5959 and P41 RR0 9784.

0740-3194/97 $3.00

time to less than 15 min, and (e) to integrate display strategies to make effective use of the isotropic image volumes. Extension of these same techniques to higher resolution (MR microscopy) is straightforward, driven primarily by limiting the field-of-view to smaller volumes.

METHODS

In the design of acquisition schemes, special attention to the problems of MR microscopy affects the number of RF excitations and specific *k*-space trajectories chosen. To keep the effective echo as short as possible, it is necessary to assume a trajectory that starts at the center of *k*-space. A number of strategies have been proposed for traversing *k*-space using trajectories that are efficient in sampling three dimensions (9). Instead, we chose a simple radial trajectory, referred to as a radial acquisition (RA) for four reasons: (a) it oversamples the center of *k*-space, effectively minimizing (cardiac) motion artifacts; (b) it provides the most efficient use of gradients; (c) it minimizes the consequences of diffusion; and (d) artifacts that do arise from motion are effectively moved outside the image space. Radial acquisition is distinguished from the less specific term of projection acquisition, which sometimes includes more complex trajectories.

The Nyquist criterion requires the sampling density on the surface of the sphere to be sufficient to support reconstruction on a matrix of N^3. The sampling density is greatest at the center of *k*-space (N^2) and varies as $1/k_r^2$, where k_r is the radial distance from the center of *k*-space. For this work, the trajectories were chosen to uniformly sample the surface of the sphere at the highest frequency (k_{max}) (10). This requires a total of 50,640 views for a 128^3 array and 204,196 for a 256^3 array.

The pulse sequence allows the scanner to run at a very short repetition time, *TR*. By streamlining the pulse-sequence code, we were able to achieve a *TR* of 3.6 ms. Figure 1 shows a schematic of the pulse sequence. The spins are excited by an α pulse with 160 μs delay before the first point of the FID is sampled. Sampling along the trajectory, k_r, is nonuniform during the rising part of the gradients (~300 μsec) and uniform after the gradients have achieved their maximum amplitude. Views are randomized using a simple relation between the view

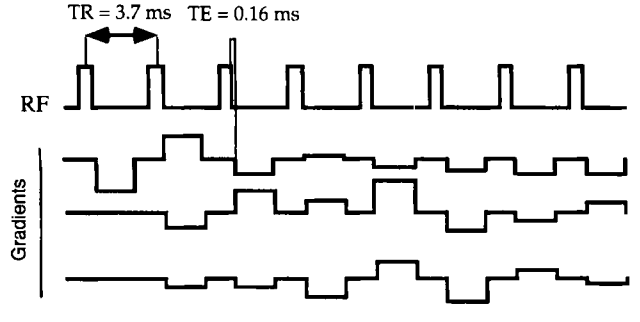

FIG. 1. The "simplicity" of the three-dimensional RA sequence permits reduction of the effective echo to <200 μs and reduction of the repetition time to <4 ms.

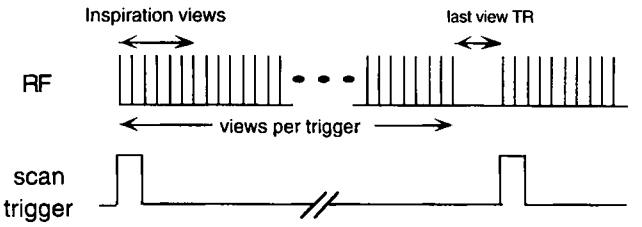

FIG. 2. A DC pulse from the ventilator at the start of inspiration triggers imaging to start. The series of views during inspiration may or may not be excluded from the image.

counter, v, and the view-to-be-taken, acview, that is

$$\text{acview} = (v^*M) \bmod \text{nviews} \qquad [1]$$

where nviews is the total number of views. The number *M* can be any integer that contains no factors of nviews. In practice, we use a prime number $M = 113$. This mixes the views, but ensures that each of the views will be taken once.

One might assume that views acquired during the expiratory phase of the ventilatory cycle might produce artifacts or blur in the image because the motion of the thoracic cavity is greatest during this period. Figure 2 shows the relationship between the ventilatory trigger and the discarded views. The ventilator starts the image acquisition at inspiration. The duration of inspiration is typically 200–400 ms, during which the scanner pulses to maintain equilibrium but the view counter is not advanced. After inspiration, view acquisition continues either with or without randomization, while the lung is at end-expiratory volume. Because a fixed number of views are played out between triggers from the ventilator, and because this view acquisition period need not be an integer multiple of *TR*, the delay between the last pulse of a given cycle and the first pulse of the next breathing cycle may be longer than *TR*. The first few alpha pulses of the next breathing cycle reestablish the equilibrium magnetization, thus limiting the view-to-view variations.

Adult guinea pigs (250–350 g, Hartley, Charles River Lab, Wilmington, MA) were anesthetized with methohexital (45 mg/kg intraperitoneal injection (IP), Brevital, Lilly, Indianapolis, IN) and given atropine sulfate (0.35 mg/kg, IP Vedco, St. Joseph, MO). The animal study protocol conformed to Duke University Animal Care and Use Committee-approved procedures. A 14-gauge endotracheal tube was inserted by tracheostomy and 2 silk ligatures around the trachea ensured a gas-tight airway connection to the ventilator. For ventilation, we used a custom-built ventilator and MRI-compatible breathing valves that were attached directly to the endotracheal tube. The breathing valves were controlled pneumatically by electropneumatic valves, which, in turn, were controlled by a LabVIEW application and a digital output board (TIO-10, National Instruments, Inc. Austin, TX) on a Macintosh computer (Apple Computer, Cupertino, CA). This system allowed independent control over the time of inspiratory gas flow and duration of held breath, as well as the timing of exhalation (11). The ventilator computer generated a DC pulse to trigger imaging acquisition

at selected points of the breathing cycle. Breathing tidal volumes were 3–4 cc and breathing rates ranged from 45 to 60/min. Cardiac activity was monitored using ECG electrodes taped to the foot pads, body temperature was measured by a rectal thermistor, and airway pressure was measured with a solid-state pressure transducer on the breathing valve. Physiological and instrument parameters were displayed with LabVIEW on the Macintosh computer.

All imaging was performed on a 2.0 T 30-cm-diameter horizontal imaging system developed explicitly for MR microscopy. The system employs 15-cm-inside-diameter shielded gradient coils, yielding a maximum gradient of 18 Gauss/cm with rise times of <300 μs. The system is controlled by a GE Signa console running version 5.4 software (GE Medical Systems, Milwaukee, WI) adapted to our magnet via an intermediate frequency stage that up-converts excitation waveforms and down-converts received signals, mixing with a frequency supplied by an external synthesizer (PTS, Program Test Sources, Inc., Littleton, MA). The resulting system appears to the user as a narrow band single-frequency system. The system can be tuned over a broad range using the external synthesizer.

The three-dimensional acquisition sequence can be used either with or without slice selection; however, the use of slice-selective excitation increases the minimum *TR* that can be achieved from 3.6–6 ms. Because our goal is optimizing general studies of pulmonary disease models, a volume coil was constructed for imaging the thorax without the use of slice selection. The coil is a "short" volume coil designed specifically for full-lung coverage in a 200–400-g guinea pig covering a 50-mm field-of-view. The coil is a modified low pass birdcage coil, 60 mm in diameter but only 40 mm long. By reducing the longitudinal dimension of the coil, the initial excitation is limited to a 50-mm cylinder well suited to imaging the entire thorax. The coil was etched on microwave substrate with distributed capacitance in the design, limiting dielectric loading. The coil employs inductive balanced coupling.

Eight guinea pigs were studied to optimize the sequence, ventilator, and coil, and to find an optimal flip angle for the lung. Pulse-repetition time and excitation were optimized using three-dimensional data sets from six animals acquired on 128^3 image matrices reconstructed from 50,640 radial views. Data were acquired for *TR* ranging between 4 and 20 ms with α ranging from 0–90°. Replicate data were acquired on two different animals at *TR* = 7 ms to verify reproducibility between animals.

Higher-resolution data were acquired on 256^3 arrays reconstructed from 204,196 views to determine the relative impact of scan-synchronous ventilation, randomization, and view discarding. All data were acquired using scan-synchronous ventilation. Comparisons were made of the images based on the following: (a) with view discarding and view randomization, (b) with view discarding and no randomization, and (c) with no randomization and no view discarding.

RESULTS/DISCUSSION

With the short *TR* used in these studies, the spins cannot recover fully. It is possible, in principle, to optimize the SNR for the *TR* by choosing an appropriate flip angle. If there is a single T_1 and it is known, then the optimal flip angle is the Ernst angle

$$\alpha_{Ernst} = \arccos(\exp(-TR/T_1)) \quad [2]$$

$S(\alpha)$, the signal as a function of α, is given by Eq. [3], where S_0 is the equilibrium signal. If T_1 is not known, then $S(\alpha)$ can be measured and T_1 determined.

$$S(\alpha) = \frac{S_0 \sin \alpha(1 - e^{-(TR/T_1)})}{1 - \cos \alpha(e^{-(TR/T_1)})} \quad [3]$$

We determined T_1 for lung as follows. Figure 3 shows the average signal from 1000, 10 × 10 regions-of-interest from the lungs of six guinea pigs as a function of α, for *TR* of 4, 7, 10, and 20 ms. The regions-of-interest were chosen to avoid large vessels and airways. Each data point represents measurements from at least two guinea pigs, except for the *TR* = 10 ms data, where the measurements from two animals are plotted separately. The data points for each *TR* were fitted to Eq. [3] using a nonlinear exhaustive search algorithm with adjustable parameters S_0 and T_1. The mean of the T_1 values obtained from the fits was 780 ms, with a standard deviation of 54 ms. The four curves drawn in Fig. 3 [$S(\alpha)$] use the individual fitted values of S_0 for each *TR* and the mean T_1 in Eq. [3]. These theoretical curves fit well and show that a single effective T_1 describes all of the data. This T_1 could be the result of averaging of several different species through fast exchange or the result of the homogeneity of the lung tissue, itself. The data do not support the existence of multiple tissue species with T_1 very different from 780 ms. The ability to describe lung tissue by a single effective T_1 allows calculation of the Ernst angle for any *TR* with Eq. [2].

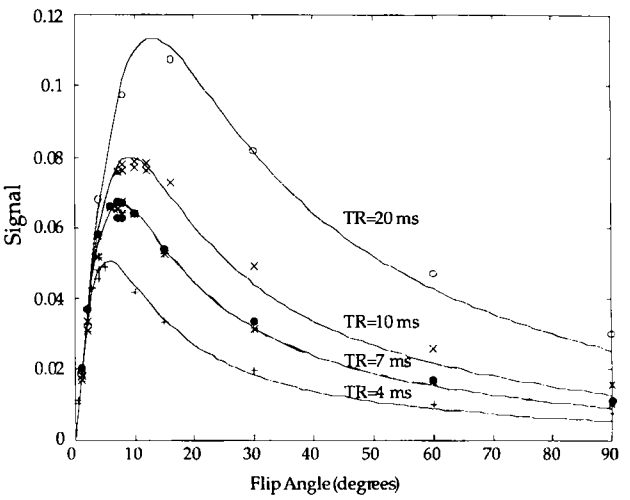

FIG. 3. Signal from the lung as a function of α is shown for 1000, 10 × 10 regions-of-interest from lungs of six guinea pigs at different angles, α, and 4 *TR*s. The solid lines are a plot from Eq. [3] using a T1 of 780 ms.

To test our calculated T_1 value, we acquired images at several flip angles. Figure 4 shows a single slice from a guinea pig at TR = 10 ms for α = 2–60°. This figure shows the contrast available by varying α. The Ernst angle is ~9° for TR = 10 ms at T_1 of 780 ms. As shown in Fig. 4, images acquired at 8–12° are consistent with our calculation, as they have the best SNR. SNR was measured in the lung parenchyma in axial slices from a 256^3 acquired at TR = 3.6 ms, α = 6°. Views during the expiratory phase of respiration were excluded. The SNR ranged from a low of 30:1 to a high of 50:1.

To best demonstrate the consequences of motion, coronal views were used, as shown in Fig. 5. These images show consequences of view randomization as well as the effects of discarding views. The greatest motion in a lung study occurs in the region near diaphragm, primarily along the longitudinal axis. The data are from isotropic 256^3 arrays. In these particular images, 12 contiguous slices are combined by direct volume rendering (VoxelView, Vital Images, Fairfield, IA) to represent the central 3 mm through a dorsal level of the thorax. Figure 5a represents an optimal imaging strategy, where views have been randomized and acquired only during expiration. Figure 5b shows the same animal where views are acquired during expiration but were not randomized. There is very little difference between the two. However, in the outer part of the left lung, note a subtle difference in the small vessel (arrow). The vessel is more clearly seen in Fig. 5a, where the views are randomized. But the detail of major structures such as liver, vena cava, peribronchial vessels, and chest wall in both Figs. 5a and 5b is excellent.

Images incorporating views acquired during both inspiration and expiration are shown in Figs. 5c and 5d. Views are randomized in Fig. 5d, but not in Fig. 5c. Again, view randomization seems to have little effect. But comparison of Figs. 5a and 5b with 5c and 5d dramatically demonstrates the consequences of discarding views acquired during inspiration. The vascular detail in the two figures with discarded views (Figs. 5a and 5b) is much clearer. Note also the distinct edge formed between the diaphragm and lung field and the loss of edge sharpness in the other images.

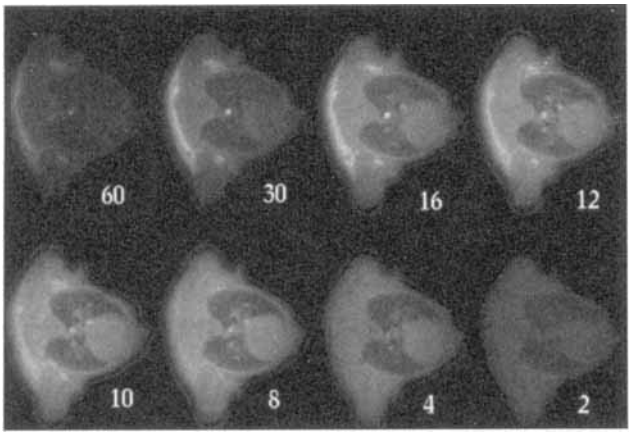

FIG. 4. A single axial slice from one guinea pig at TR = 10 ms for α = 2–60°, showing the contrast available by varying α.

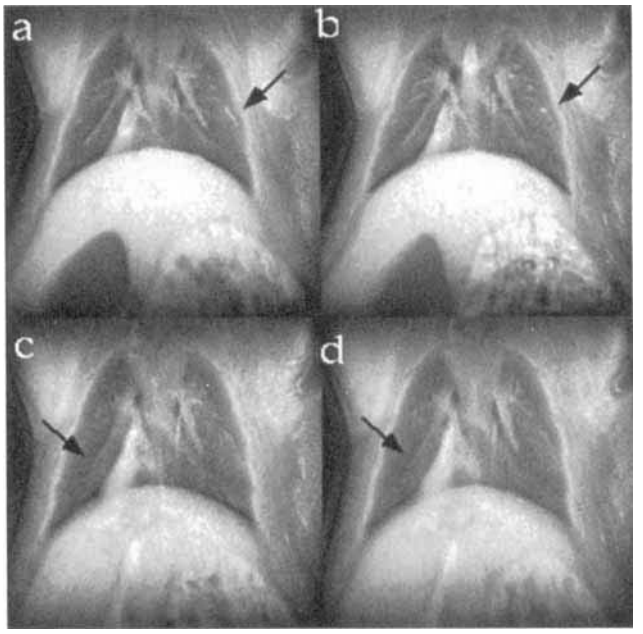

FIG. 5. Volume-rendered 3-mm-thick slices from 256^3 arrays demonstrate the effects of view under randomization and discarding views during inspiration: (a) Views discarded during inspiration and randomization. (b) With views discarded and no randomization. (c) Without discarding views and with randomization. (d) Without discarding views and no randomization. Effects of view under acquisition (random versus nonrandom) are clearly seen by comparing the small pulmonary vessel in a and b and the lobar bronchus in c and d (arrows). In each case, there is better structural definition with randomization than without.

CONCLUSION

We have refined three-dimensional projection encoding explicitly for application in MR microscopy of the lung in small animals. We have integrated an RF coil specifically for lung imaging with a pulse sequence for rapid acquisition (TR < 4 ms). The three-dimensional sequence has been optimized to allow collection of isotropic 256^3 arrays in less than 15 min. The scheme represents a substantial improvement over our previous two-dimensional efforts that had scan-time constraints imposed by cardiac gating and slice resolution (1 mm) constrained by slice-selection requirements. In the current study, breathing motion has been minimized through the use of scan-synchronous ventilation. By excluding views acquired during the inspiratory phase of breathing, we have accomplished high resolution. View variations due to motion are minimized by maintaining the equilibrium magnetization during the entire breathing cycle without advancing the view counter. Unexpectedly, randomization of views has limited effect.

Our first efforts at MR microscopy of the lung were published more than 10 years ago (12). Steady technical progress has allowed us to increase the spatial resolution from 0.235 × 0.235 × 2.0 mm (i.e., 0.10 mm^3) to 0.235^3 mm (i.e., 0.013 mm^3), while simultaneously reducing the acquisition time eightfold. Improvement in SNR in this work comes from a combination of specific coil and pulse sequence tied together. The coil contributes ~ a factor of twofold improvement over our previous work

arising from the improved filling factor. For a T_2 of 5 ms, typical of what we measure in the rat lung, one would expect an improvement of ~ 6X as one reduces *TE* from 2 ms to 0.2 ms. Finally there is additional improvement (< factor of 2) arising from the centric sampling that it used. The major barriers to date have been effective control of motion, the development of efficient pulse sequences, and the continuing limitation posed by limited signal at microscopic resolution. The work reported here represents major advances beyond these barriers. Further increases in spatial resolution are already contemplated through the use of high-temperature superconducting receivers (13) and the use of hyperpolarized gas (14). The most challenging organ, the lung, is now routinely accessible by MR microscopy.

ACKNOWLEDGMENTS

The authors thank Gary P. Cofer for technical assistance and Elaine G. Fitzsimons for editorial assistance.

REFERENCES

1. M. Rudin, W. Zierhut, A. Sauter, N. Cook, New developments in cardiovascular magnetic resonance imaging and spectroscopy. *Trends Pharmacolog. Sci.* **12,** 416–421 (1991).
2. R. M. Summers, L. W. Hedlund, G. P. Cofer, M. B. Gottsman, J. F. Manibo, G. A. Johnson, MR microscopy of the rat carotid artery after balloon injury using an implanted coil. *Magn. Reson. Med.* **33,** 785–789 (1995).
3. C. H. Burney, J. Bertolina, D. C. Ailion, Calculation and interpretation of inhomogeneous line broadening in models of lung and other heterogeneous structures. *J. Magn. Reson.* **85,** 554–570 (1989).
4. C. J. Bergin, G. H. Glover, J. M. Pauly, Lung parenchyma: magnetic susceptibility in MR imaging. *Radiology* **180,** 845–848 (1991).
5. S. L. Gewalt, G. H. Glover, J. R. MacFall, L. W. Hedlund, G. A. Johnson, MR microscopy of the rat lung using projection reconstruction. *Magn. Reson. Med.* **29,** 99–106 (1993).
6. C. M. Lai, P. C. Lauterbur, True three-dimensional image reconstruction by nuclear magnetic resonance zeugmatography. *Phys. Med. Biol.* **26,** 851–856 (1981).
7. G. Glover, J. Pauly, Projection reconstruction techniques for reduction of motion effects in MRI, *in* "Proc., ISMRM 4th Annual Meeting, New York, 1996," p. 327.
8. C. J. Bergin, J. M. Pauly, A. Macovski, Lung parenchyma: projection reconstruction MR imaging. *Radiology* **179,** 777–781 (1991).
9. C. Meyer, B. Hu, D. Nishimura, A. Macovski, Fast spiral coronary artery imaging. *Magn. Reson. Med.* **28,** 202 (1992).
10. G. H. Glover, J. M. Pauly, K. M. Bradshaw, Boron-11 imaging with a three-dimensional reconstruction method. *J. Magn. Reson. Imaging* **2,** 47–52 (1992).
11. L. W. Hedlund, M. D. Shattuck, G. A. Johnson, Three-dimensional MR microscopy of pulmonary dynamics, *in* "Proc., ISMRM 4th Annual Meeting, New York, 1996," p. 327.
12. L. W. Hedlund, G. A. Johnson, J. P. Karis, E. L. Effmann, MR microscopy of the rat thorax. *J. Comput. Assist. Tomogr.* **10,** 948–952 (1986).
13. R. D. Black, T. A. Early, P. B. Roemer, O. M. Mueller, A. Morgo-Campero, L. G. Turner and G. A. Johnson, A high temperature superconducting receiver for NMR microscopy. *Science* **259,** 793–795, (1993).
14. R. D. Black, H. Middleton, G. D. Cates, G. P. Cofer, B. Driehuys, W. Happer, L. W. Hedlund, G. A. Johnson, M. D. Shattuck, J. Swartz, *In vivo* He-3 MR images of guinea pig lungs. *Radiology* **199,** 867–870 (1996).